

Interplay of capillary and elastic driving forces during microstructural evolution: Applications of a digital image model

Jeffrey W. Bullard

University of Illinois at Urbana-Champaign, Department of Materials Science and Engineering, Urbana, Illinois 61801

Edward J. Garboczi

Building Materials Division, National Institute of Standards and Technology, Gaithersburg, Maryland 20899

W. Craig Carter

Ceramics Division, National Institute of Standards and Technology, Gaithersburg, Maryland 20899

(Received 12 November 1997; accepted for publication 5 January 1998)

A recently developed model of curvature-driven, two-dimensional microstructure evolution is modified to include elastic strain energy at solid-fluid interfaces as an additional driving force for mass transport. Local phase distributions within a digital image of the microstructure are used to interpolate an isopotential contour that represents the equivalent sharp surface, along which local properties such as curvature are calculated. To determine the strain energy distribution, a finite element method is employed, using the pixel grid as the mesh. Interface-reaction-controlled mass transport is simulated using a finite difference approach along the interface. Calculations of the strain energy density and chemical potential distributions within simple systems show reasonable agreement with analytical results, and the predicted stability and evolution of such systems also agree with the predictions of other investigators. The model is also applied to a more complex system for which neither analytical nor other numerical methods can be readily used, and useful quantitative information is obtained on the energetics and structural changes. © 1998 American Institute of Physics. [S0021-8979(98)01408-X]

I. INTRODUCTION

In a recent article, one of the authors described a numerical method for simulating dissipative temporal evolution of two-dimensional microstructures.¹ That method models the dynamics of evolution according to partial differential equations derived from linear irreversible thermodynamics, and tracks the resulting interface motion. When the assumption is made that global interface free energy provides the only appreciable driving force, then—provided that the interface free energy density is isotropic—the local driving force for evolution is determined solely by gradients in the interfacial mean curvature.² Curvature gradients are therefore sufficient to describe the driving force for Ostwald ripening of a dispersed phase in a fluid,^{3,4} for coarsening in porous media,⁵ for high-temperature crack healing,⁶ and for the instability of long cylinders toward spheroidization.⁷

On the other hand, it has long been recognized that elastic deformation can also provide an appreciable driving force for interface motion. Charles and Hillig were perhaps the first to incorporate elastic driving forces in a description of cavity growth during static fatigue of glasses.^{8,9} Asaro and Tiller included elastic strain energy density in a description of the boundary values of the chemical potential to perform a linear stability analysis of the planar interface separating a stressed two-dimensional semi-infinite solid from a fluid.¹⁰ Rice and Chuang¹¹ found boundary values for the chemical potential for a cavity within an elastically deformed infinite solid. Grinfeld¹² and Srolovitz¹³ have both re-examined the role played by elastic deformation in determining the stabil-

ity of planar surfaces. These theoretical investigations all conclude that elastic deformation alters the boundary values of the chemical potential and, therefore, can significantly alter the rate and trajectory of interface motion.

On the basis of these considerations, it seems desirable to have a numerical model that not only can assess the stability of interface morphologies, but that also can track interface motion in microstructures under the influence of both curvature gradients and elastic deformation. Yang and Srolovitz¹⁴ used an elastic Green's function in a finite element model to simulate the evolution by surface diffusion of a periodic sinusoidal surface under these driving forces. Wang *et al.*^{15–17} have used a time-dependent Ginzburg–Landau (TDGL) model to simulate the shape evolution of coherently misfitting solid precipitates in a solid matrix when the elastic constants of both phases are the same. The latter modeling approach has the advantage that interface tracking is automatic, even during topological changes.

In this article, we extend the numerical model reported in a previous article¹ to include elastic strain energy density at solid/fluid interfaces. In contrast to the TDGL models, this model uses a sharp-interface approach rather than a diffuse interface. Nevertheless, it shares with TDGL models the advantage of automatic interface tracking and accommodation of topological changes. It also provides a clear connection between model variables and thermodynamic/kinetic parameters describing physical systems, and therefore allows one to adjust the absolute rates of different mechanisms of mass transport. And because it formulates the dynamics in terms

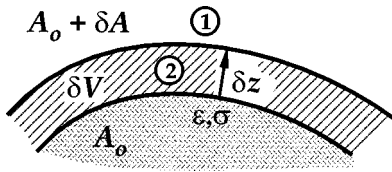


FIG. 1. Schematic illustration of the virtual motion of a solid-fluid interface by coherent deposition of a volume of solid δV , causing the local surface element to be displaced a distance δz . The work required for this deformation is assumed to be the sum of (1) the work required to form the extra surface δA , and (2) the elastic work required to make the added solid fit coherently.

of linear irreversible thermodynamics, it can be readily extended to include other possible driving forces such as thermal gradients and electric fields. This model therefore could form the basis for a processing design tool that, in conjunction with limited experimental studies, might be used to determine optimal processing routes for obtaining desired microstructures.

In the next section, we describe the hybrid numerical method for computing boundary values of the chemical potential and for simulating the dynamics of interface motion. We then give examples that illustrate some of the advantages—and limitations—of the current model. Finally, we outline some approaches that are underway for improving the accuracy of the chemical potential calculation.

II. DRIVING FORCE: CURVATURE AND ELASTIC ENERGY DENSITY

Driving forces for interface motion under the combined influences of mean curvature and elastic energy density have been derived elsewhere with varying degrees of rigor.^{8–13} All of these derivations assume that single-component interface motion occurs by coherent dissolution to and coherent precipitation from a fluid of the same composition as the solid, and they all arrive at essentially the same expression for the boundary value of the chemical potential. To motivate that expression, consider the isothermal work per mole performed in coherently precipitating a solid layer of thickness δz onto a small interfacial element. That work may be expressed as the sum of (1) the incremental work required to displace the interface and (2) the deformation work required to make the solid fit coherently (see Fig. 1). The first component of the sum is

$$\delta W_1 = \gamma \delta A = \gamma \frac{\partial A}{\partial V} \frac{\partial V}{\partial z} \delta z = \gamma \kappa A_0 \delta z, \quad (1)$$

where γ is the interfacial free energy density (assumed to be isotropic), δA is the incremental change in the interface element, of initial area A_0 , accompanying its normal displacement by δz , and κ is the mean curvature of the interfacial element. The second component to the work is given by

$$\delta W_2 = \int_{\delta V} \sigma_{ij} \epsilon_{ij} dV.$$

If the precipitated volume, δV is small enough, and if it can be considered to be deformed homogeneously and quasistati-

cally, then we may consider the components of the stress and strain tensors σ_{ij} and ϵ_{ij} as constant averaged quantities over its volume, δV , so that

$$\begin{aligned} \delta W_2 &= \frac{1}{2} \sigma_{ij} \epsilon_{ij} \delta V = \frac{1}{2} \frac{\partial V}{\partial z} \sigma_{ij} \epsilon_{ij} \delta z, \\ &= \frac{1}{2} A_0 \hat{\sigma} : \hat{\epsilon} \delta z. \end{aligned} \quad (2)$$

Combining Eqs. (1) and (2) gives

$$\delta W = \left[\gamma \kappa + \frac{1}{2} \hat{\sigma} : \hat{\epsilon} \right] A_0 \delta z = \left[\gamma \kappa + \frac{1}{2} \hat{\sigma} : \hat{\epsilon} \right] \Omega \delta N, \quad (3)$$

where Ω is the molar volume of the deposited material, and δN is the number of moles deposited. With the above assumptions, this incremental work is equal to the incremental change in the Helmholtz free energy of the deposited material, and the bracketed quantity on the right side of Eq. (3) can be immediately identified as the difference in chemical potential between the fluid and the adjacent solid. Therefore,

$$\begin{aligned} \mu &= \mu^0 + \left[\gamma \Omega \kappa + \frac{1}{2} \Omega \hat{\sigma} : \hat{\epsilon} \right], \\ &= \mu^0 + \Omega \left[\gamma \kappa + \frac{1}{2} \hat{\epsilon} : \hat{C} : \hat{\epsilon} \right], \end{aligned} \quad (4)$$

where μ^0 is the chemical potential of the relaxed solid in equilibrium with a zero-curvature interface. The last form arises from assuming linear elasticity, with stiffness tensor \hat{C} . Although Eq. (4) is general enough to include elastic anisotropy, we use an isotropic stiffness tensor in this article.

Note that Eq. (4) is a valid expression for the chemical potential only along single-component solid-fluid interfaces that are isotropic in γ . The relative magnitudes of the second and third terms on the right side of Eq. (4) have a strong influence on the distribution of chemical potential along such interfaces, and a rich variety of interface motions are accessible from this restricted equation. Throughout the remainder of this article we will use Eq. (4) to compute the driving force for interface motion and, consequently, restrict our attention to those types of interfaces for which Eq. (4) is valid. We therefore do not consider solid-solid interfaces like grain boundaries and interphase boundaries.

III. COMPUTATIONAL METHODS

The numerical method uses a digital image to model a microstructure. That is, the image of a portion of a heterogeneous microstructure is mapped onto a regular lattice of 2D square or 3D cubic elements (pixels). Each element in the lattice is assigned the thermodynamic properties of the phase corresponding to its position in the original microstructural image. Digital images can therefore reproduce 2D or 3D microstructures of virtually arbitrary complexity, although in this article we restrict attention to 2D microstructures. Furthermore, the discretization reduces the problem of calculating continuum microstructural evolution to that of evaluating small changes in the local pixel environment. The relative size of a microstructure that can be stored this way—that is,

the size of the microstructure divided by the size of the minimum resolvable microstructural feature—is somewhat limited by the computer's memory capacity. Even so, on a high-performance work station one can easily accommodate ratios of at least 100–1000 in 2D.

The pixels comprising the microstructure image are treated as continuum 2D “volume” elements characterized by a parameter, η , that defines the fraction of each phase within that element. In the general case of an n -phase system, one could think of η as an n tuple, or a vector in an orthogonal n space, with each vector component defining the phase fraction of a different phase. For a microstructure composed of a single-component solid phase and an otherwise inert fluid containing that component, which is the microstructure type that we will focus on in this paper, η may be thought of as a scalar defining the area fraction of the pixel occupied by the solid phase ($0 \leq \eta \leq 1$). Mass transport mechanisms and rates are fixed by specifying a range of pixel exchange interactions and employing finite difference algorithms to approximate the partial differential equations (PDEs) describing the time rate of change of η within each pixel.

One other advantage of the digital-image approach is that, in addition to approximating PDEs by finite difference methods, it is possible to devise efficient numerical routines to compute physical quantities that determine the local driving force for interface motion within the microstructure. We use two such algorithms in the present simulations, one to compute local interface curvature and one to determine the elastic strain energy density field. Both of these algorithms have been described in considerable detail elsewhere,^{1,18} and they will be only briefly outlined here.

A. Mean curvature

The algorithm used to compute curvature has been described in Ref. 1. It is based on the concept of approximating the interface between two phases by linearly interpolating an isopotential contour, or level set, through a 2D or 3D point set (the η -values assigned to the center of each pixel element). We refer to this level set as the equivalent sharp surface (ESS). A particular value of η is selected as the interpolation point, usually 0.5 for a two-phase system. The level set is thus composed of connected line segments in 2D. Methods for constructing 2D level sets from 3D point sets have been published,¹⁹ so there is no conceptual difficulty in extending the method to three dimensions.

Having constructed the ESS for a given microstructural image, the unit outward normal vector \mathbf{n} for each segment can be easily determined from vector algebra. Then the discrete approximation to the mean curvature κ of that portion of the interface can be calculated according to

$$\kappa = \nabla_s \cdot \mathbf{n} \quad (5)$$

by using numerical differentiation to compute the surface divergence.

B. Elastic energy density

We assume plane-stress elasticity, and use the pixel grid of the digital image to define a finite element mesh, the

nodes of which are located at the pixel corners. The displacement field $\mathbf{u}(x,y)$ is approximated using a standard finite element expansion for a four-noded element,

$$u_i(x,y) = u_i^{sw} + \left(\frac{u_i^{se} - u_i^{sw}}{\xi} \right) x + \left(\frac{u_i^{nw} - u_i^{sw}}{\xi} \right) y + \left(\frac{u_i^{ne} + u_i^{sw} - u_i^{se} - u_i^{nw}}{\xi^2} \right) xy,$$

where u_i^{sw} , for example, is the value of the i -direction displacement at the southwest (lower lefthand corner) node of the square element, i indicates either the x or y component of the displacement, ξ is the edge length of the square element in the reference state, and x and y are continuous variables with respect to a local coordinate system having the southwest node as its origin.

After specifying the mechanical conditions at each of the periodic boundaries of the system (in these simulations, we used either fixed grips, fixed displacement rate, or fixed tractions along the boundaries), the equilibrium nodal displacements are computed by minimizing the linear elastic strain energy, according to a fast conjugate gradient algorithm written specifically to operate on regular square element meshes with periodic boundary conditions.¹⁸ Since this is an iterative solver, one must specify a maximum value for the total energy gradient below which the system is considered to be relaxed. For these simulations, the maximum gradient is set to 10^{-9} times the number of elements.

There is some question as to how the elastic constants of a given pixel should depend on the value of η within that pixel. Certainly when $\eta=1$ and 0, the bulk and shear moduli are equal to those of the solid and fluid phase, respectively. An appropriate functional dependence of the elastic constants on η for $0 < \eta < 1$ is not readily apparent, however. In a composite medium, the effective elastic constants depend not only on the fraction of each phase present, but also on the spatial distribution of those phases relative to the applied load. Thus a rigorously correct choice for the elastic constants of a given pixel requires knowledge of the phase distribution within that pixel. In this article, we sacrifice some accuracy for the sake of considerable numerical efficiency by assigning to each pixel

$$(K, G) = \begin{cases} (K_f, G_f) & \eta < \eta^*, \\ (K_s, G_s) & \eta \geq \eta^*, \end{cases}$$

where K is the bulk modulus, G is the shear modulus, the subscripts f and s denote fluid and solid, respectively. The cutoff value, η^* , is chosen as the value that produces the closest agreement between numerical calculation and the analytical prediction of the strain energy distribution along the surface of a circular hole in a uniaxially strained homogeneous sheet. We determine the value of η^* in the simulation results (Sec. IV) and, in the discussion (Sec. V), we describe a potentially more accurate method that is currently under scrutiny.

By averaging the equilibrium nodal strains of a given pixel P , we compute the average strain within P . The aver-

age elastic strain energy density in each pixel is calculated, assuming linear elasticity, and is used in Eq. (4) to determine the elastic contribution to the chemical potential.

C. Kinetics

In general, gradients in the boundary values of the chemical potential will drive a redistribution of material. This redistribution may be accomplished by one or more of several possible transport paths/mechanisms. In this numerical framework, a given rate-controlling step is modeled by its corresponding continuum rate equation, which is approximated by a finite difference formulation and adaptively integrated forward in time using a maximum dimensionless time step of Δt , which we set to unity for convenience.

The simulations presented in this article were all performed using surface-attachment-limited kinetics (SALK), by which it is assumed that diffusion rates are much greater than the rate of coherent accretion/dissolution of matter at the interface. With this assumption it may readily be shown¹ that the net rate of accretion per unit area, J , at any point x along the interface is

$$J(x) \equiv \frac{dN}{dt} = \frac{k_{\text{SALK}}}{RT} [\mu^{\text{amb}} - \mu(x)], \quad (6)$$

where k_{SALK} is the reaction rate constant, R is the gas constant, T the absolute temperature, and μ^{amb} is the ambient chemical potential of diffusing species in the fluid phase, which is approximately constant when diffusion is very fast compared to equilibration with the interface. Each term in Eq. (6) is made dimensionless by scaling time and length values to the reaction rate constant and pixel edge length (see Appendix A for a table of all dimensionless quantities used in this article). Equation (6) is then discretized to give

$$\Delta \eta_p = C[\mu^{\text{amb}} - \mu_p] S_p \Delta t, \quad (7)$$

where η_p is the solid volume fraction located within pixel P , C is a dimensionless rate constant, and S_p is the (dimensionless) length of interface associated with the P th pixel.

The value of μ^{amb} that conserves mass can be calculated as the mean value of μ over the entire set of interfaces, Γ :

$$\bar{\mu} = \frac{\int_{\Gamma} \mu dS}{\int_{\Gamma} dS}.$$

Setting μ^{amb} greater/less than $\bar{\mu}$ will cause a monotonic increase/decrease in solid mass.

IV. SIMULATION RESULTS

All quantities used in the remainder of this article have been made dimensionless (see Appendix A for the conversions).

A. Determination of η^*

As mentioned in the previous section, we choose a cutoff value for η , above which a pixel is assigned the elastic properties of the solid. To determine a reasonable value for η^* , we numerically calculate, for different trial values of η^* , the elastic strain energy density distribution along the surface of a circular cavity in a uniaxially strained sheet, and compare

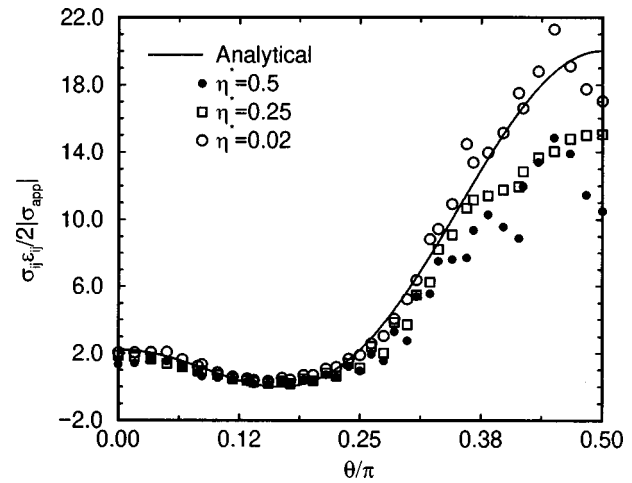


FIG. 2. Distribution of elastic strain energy density along the upper right quadrant of a circular cavity in a homogeneous sheet subjected to an applied stress, σ_{app} in the y direction. θ is the interior angle between the x axis and the radial position vector whose origin is at the center of the cavity.

to the analytical result, as shown in Fig. 2. The value of η^* that most closely reproduces the analytical curve is 0.02, and so that value is used to obtain the following results. We will return later to some of the implications of choosing this value.

B. Chemical potential along a sinusoidal interface

To find an indication of how accurately the numerical method calculates chemical potential, we compare our numerical results to an analytical prediction for a shallow sinusoidal perturbation in a 2D solid that is thick compared to the amplitude of the perturbation. We choose a relatively small system, 101×51 pixels to conduct the test, with periodic boundary conditions in x , and a tensile stress $\sigma_{xx} = \sigma_0$. The interface is given by $y = a \cos 2\pi x/\lambda$, with $a = 5$ and $\lambda = 100$.

Analytical expressions for the stress components along the surface of a sine wave under uniaxial tension are known¹⁰ and may be used to calculate the boundary values of the strain energy density (see Appendix B).

At fixed applied stress and surface geometry, the magnitude of the elastic term relative to the curvature term in Eq. (4) is determined by the dimensionless ratio $\Sigma = \sigma_0 \sqrt{L/E} \gamma$, where E is the Young's modulus of the solid and L is a characteristic length that sets the scale of the system.¹³ We take $L = \lambda$, the wavelength of the perturbation. Numerical and analytical values for the chemical potential are shown in Fig. 3 for two values of this ratio. When the curvature term dominates [$\Sigma = 1$, see Fig. 3(a)], the numerical values are somewhat scattered about the analytical curve, reflecting pixel-to-pixel inaccuracy in the curvature calculation caused by the sawtooth geometry of the surface in the digital image. In this particular instance, the scatter seems to be about 30% of the range in values, although it must be remembered that the range in curvature values is quite small for such a shallow sine wave. The relative accuracy in the curvature is greater when the range of curvatures is wider. In any event, the ESS method for calculating curvature is substantially

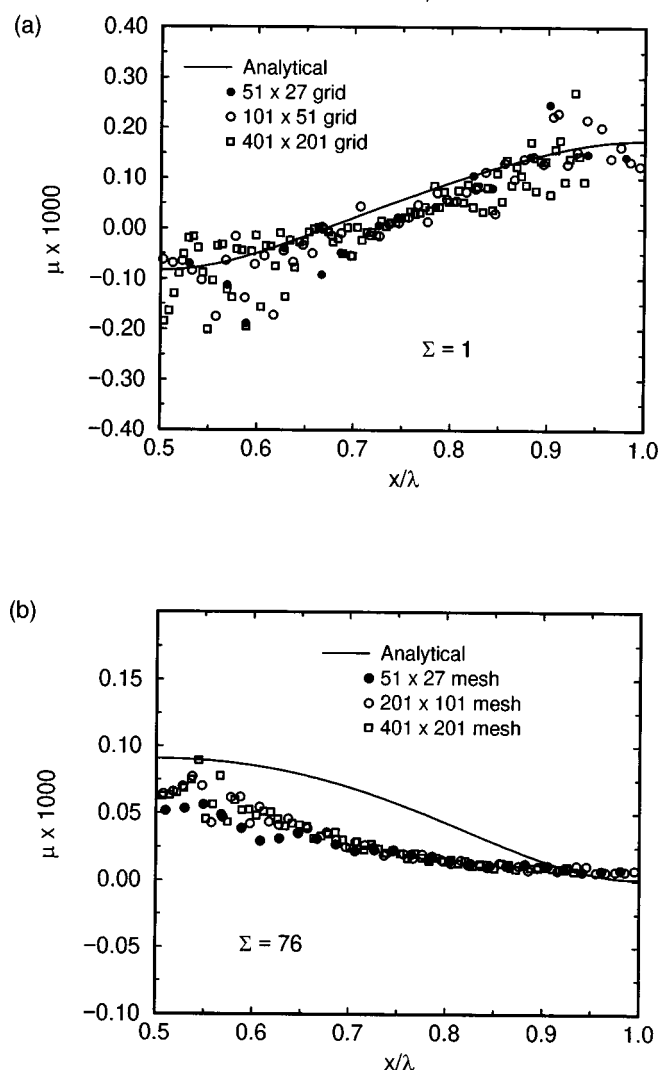


FIG. 3. Comparison of numerical computation of dimensionless chemical potential to analytical results (solid lines), showing the effect of grid resolution. λ is the wavelength of the sinusoidal perturbation that is under tension in the x direction. (a) $\Sigma=1$, and (b) $\Sigma=76$.

more accurate than alternative methods for digital images,²⁰ and the effect of the local scatter on the predicted dynamics of evolution has been previously shown to be quite small.¹

When the elastic term in Eq. (4) dominates [$\Sigma=76$ in Fig. 3(b)], the numerical calculations underestimate the analytical curve except at $x/\lambda=0$ and 1, where it slightly overestimates the analytical values. This is an artifact of having chosen a single step-function dependence of stiffness on η , which causes the finite element algorithm to interpret the interface as being terraced. At the shallow amplitudes used in this example, the terraces are fairly long, and the effect is to flatten out the strain energy distribution. This interpretation is supported by the calculated strain energy density along a circle shown in Fig. 2; the curve for $\eta=0.02$ fits the analytical curve quite closely along most of the circle, except near $\pi/2$ where the surface is approximated as a long flat terrace.

Compared with other applications of finite element/finite difference methods, one might not expect grid refinement to

substantially improve numerical convergence to an analytical result. As already noted, the underlying digital image causes interfaces to have a sawtooth shape and, while the curvature calculation is more accurate by the ESS algorithm than by other methods for digital images,^{1,20} the terraced nature of surfaces cannot be eliminated by the former method. For the finite element calculations of elastic strain energy density, the step-function dependence of the elastic moduli on η also causes a sawtooth surface geometry. Therefore, even with grid refinement surfaces are still composed of ledges and terraces, and one can expect a finite amount of local scatter in surface quantities, like boundary values of chemical potential.

To test the convergence of the numerical solution, simulations were conducted on the same sine wave using pixel grids of 51×27 , 101×51 , 201×101 , and 401×201 . The calculated chemical potentials are shown in Figs. 3(a) and 3(b). It is clear that grid refinement has, at best, a weak effect on convergence to the analytical curve, since the local scatter is not appreciably reduced with increasing resolution. Later, in the discussion, possibilities for further improving numerical convergence will be addressed. It will become evident in the next section, however, that the local scatter in chemical potential does not markedly affect the predicted dynamics of interface motion.

C. Evolution of a sinusoidal perturbation

Referring to Fig. 3, it is clear that the position of maximum chemical potential shifts from the crest of the surface, at low applied stresses, to the valley at higher stresses. Therefore, at low applied stresses, mass should flow from the crest to the valley, causing a decrease in amplitude. At higher stresses, mass should flow from the valley to the crest, and the amplitude, at least initially, should increase. As mentioned in the introduction, several investigations of the initial stability of such a perturbation toward amplitude changes have been published.^{10,12,13} Of these, only Srolovitz¹³ conducted a linear stability analysis for both surface diffusion kinetics and SALK (which he referred to as evaporation/condensation). His prediction for SALK is that any wave number $k > k^* = 2\sigma_{xx}^2/E\gamma$ will decay exponentially, while longer wavelengths are unstable toward growing in amplitude. In a later article¹⁴ Yang and Srolovitz simulated the evolution of a sine wave by surface diffusion and showed that at high stresses a surface instability manifested itself as the appearance and growth of a sharp cracklike feature in the valleys. We know of no prior predictions for the analogous temporal evolution by SALK, which we now present.

To facilitate a comparison with the results of Yang and Srolovitz,¹⁴ we report results in units of scaled stress, $\Sigma = \sigma_0 \sqrt{\lambda/\gamma E}$ and scaled time, $\tau = \lambda^2/(C\gamma)$ [C is the dimensionless rate constant from Eq. (7)]. Figure 4 shows the evolution by SALK when $\Sigma=2.5$. The amplitude slowly increases at first, and then at $t \approx 1.7 \times 10^{-3} \tau$, a groove begins to form in the valley. The groove sharpens and extends further into the solid with time due to the increasing strain energy at the tip. We do not, however, identify the groove as a “crack”. Whereas growth of a crack can occur when the local stress exceeds the bond strength, the formation of the

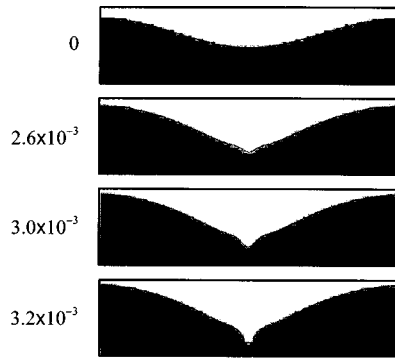


FIG. 4. Evolution by SALK of a sinusoidally perturbed interface for $\Sigma=2.5$. The ratio of initial amplitude to wavelength is $a_0/\lambda=0.05$. Times shown at left are in terms of τ .

groove in Fig. 4 occurs as a result of a local maximum in chemical potential, and its growth occurs by material transport over distances that are large compared to atomic dimensions. Furthermore, the length scale of a crack tip is of atomic dimensions, and we can claim no such absolute dimensions for the groove tip since, according to the continuum formulation of the model, the minimum length scale is set by the grid resolution ξ .

Figure 5 shows, for several values of Σ , the time dependence of the maximum height difference, h , scaled by the initial amplitude of the sinusoidal surface. The stress-free dynamics ($\Sigma=0$) corresponds very closely to that predicted by Mullins²¹ for the amplitude decay of a shallow sine wave.¹ When $a_0/\lambda \ll 1$, then

$$\frac{da}{dt} = -Ck^2a,$$

where $k=2\pi/\lambda$. Integration yields, to first order in t ²¹

$$a - a_0 = -a_0 C k^2 t, \quad (8)$$

i.e., the negative slope for the $\Sigma=0$ curve in Fig. 5 is proportional to C . Low stresses ($\Sigma=1$) lower the driving force

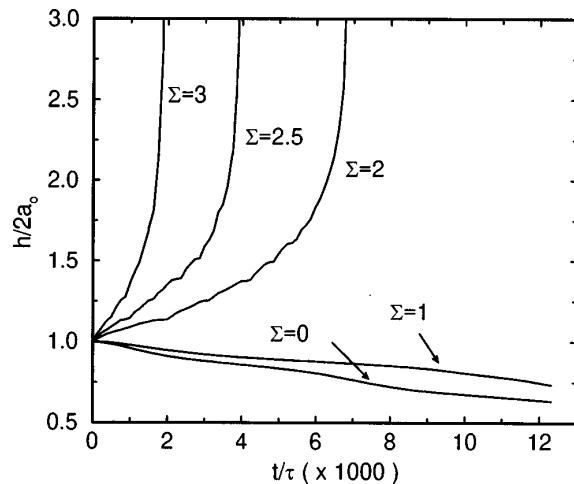


FIG. 5. Maximum height difference as a function of time for a sinusoidal surface evolving under different values of Σ . Height is normalized by the initial amplitude.

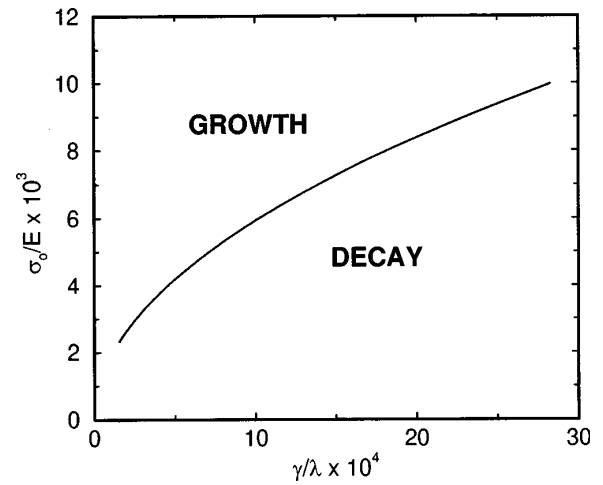


FIG. 6. Stability map for a sinusoidal surface under the influence of both capillary and elastic driving forces.

for amplitude decay, although the trajectory of evolution is still much like the stress-free trajectory. Clearly from Fig. 5, a critical value of Σ —between 1 and 2—exists for which the interface is unstable toward formation and growth of a groove in the valley. Further simulations not depicted in Fig. 5 indicate $\Sigma_c = 1.7 \pm 0.1$. This value agrees closely with that predicted by Srolovitz's linear stability analysis¹³ ($\Sigma_c = 1.77$ using the same physical constants as for these simulations).

Knowledge of Σ_c allows one to plot a map for the perturbed surface, as shown in Fig. 6, that indicates the direction of the surface instability. In Fig. 6, the ordinate values σ_0/E indicate the strength of the elastic contribution to μ , and the abscissa values γ/λ indicate the strength of the curvature contribution. The boundary curve separating the growth field from the decay field corresponds to Σ_c .

D. RANDOMLY PACKED PARTICLES

We now proceed to analysis of a more complicated system, namely a random packing of solid circles in two dimensions, shown at the top of Fig. 7. Each particle has a diameter d selected at random within a range of 11–31 pixels, and each was placed within a 160×160 box by dropping it from randomly selected locations along the top boundary, using periodic boundaries in the horizontal direction, until further displacement was prevented by contact with other particles. Once all the particles (a total of 53) were placed, yielding a solid fraction $f=0.74$, periodic boundary conditions were also enforced along the top and bottom edges. A uniaxial tensile strain ϵ_0 was applied along the horizontal direction. A side-by-side comparison of the predicted evolution using identical rate constants C is shown in Fig. 7 for $E\epsilon_0^2 L/\gamma = 0$ and 2.5; the scaled unit of time is now taken to be $\tau = L^2/(C\gamma)$ with $L=160$ being the length of the system.

When no deformation is applied to the particle system, reduction of surface free energy causes evolution toward a 2D lamellar morphology (recall that all boundaries are periodic). The presence of deformation in the x direction, on the other hand, evidently produces a strain energy distribution

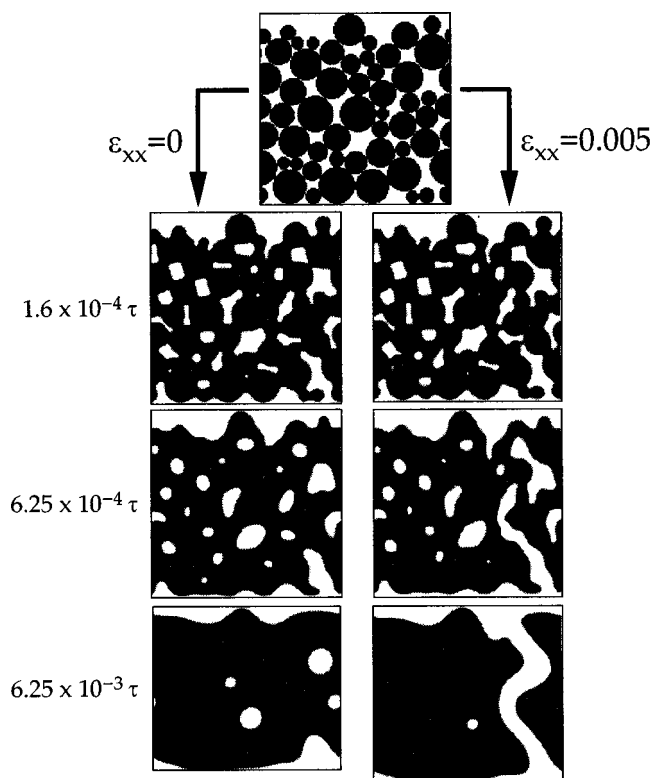


FIG. 7. Assembly of particles in a 160^2 box. Left column shows evolution of system by SALK with no applied deformation. Right column shows evolution with a tensile strain of 0.005 applied in the horizontal direction.

that makes certain of the initial interparticle contacts unstable toward attenuation and severance. As more of the contacts disappear by this instability, increasing strain energy density is shifted to the remaining load-bearing contacts, which accelerates their attenuation. This process is repeated until the solid suffers a complete division to form an isolated domain. Thus, invoking the nomenclature of Newnham *et al.*,²² deformation causes a change in the predicted connectivity of the structure from 1-1 to 0-2.

The trajectories shown in Fig. 7 are sensitively dependent, not only on the applied deformation, but also on the initial geometry. In particular, the lamellar morphology that ultimately results without deformation is entirely a result of the inhomogeneous packing near the top and bottom boundaries. A packing algorithm that allows particles to overlap those boundaries, as they do for the horizontal boundaries, would presumably result in a much more statistically isotropic microstructure. But despite this dependence on initial geometry, one might expect the gross influences of deformation—provided that it is large enough—to be qualitatively the same whether or not particle overlap along the top and bottom boundaries is allowed. The elastic strain energy density should be relatively concentrated along a band, approximately orthogonal to the loading axis, with the least load-bearing area. Propagation of cracklike flaws due to repeated neck rupture, if it occurs at all, should be observed along this band.

In addition to these qualitative influences of elastic deformation, it is possible to quantitatively assess certain aspects of the evolution in the same way as described more

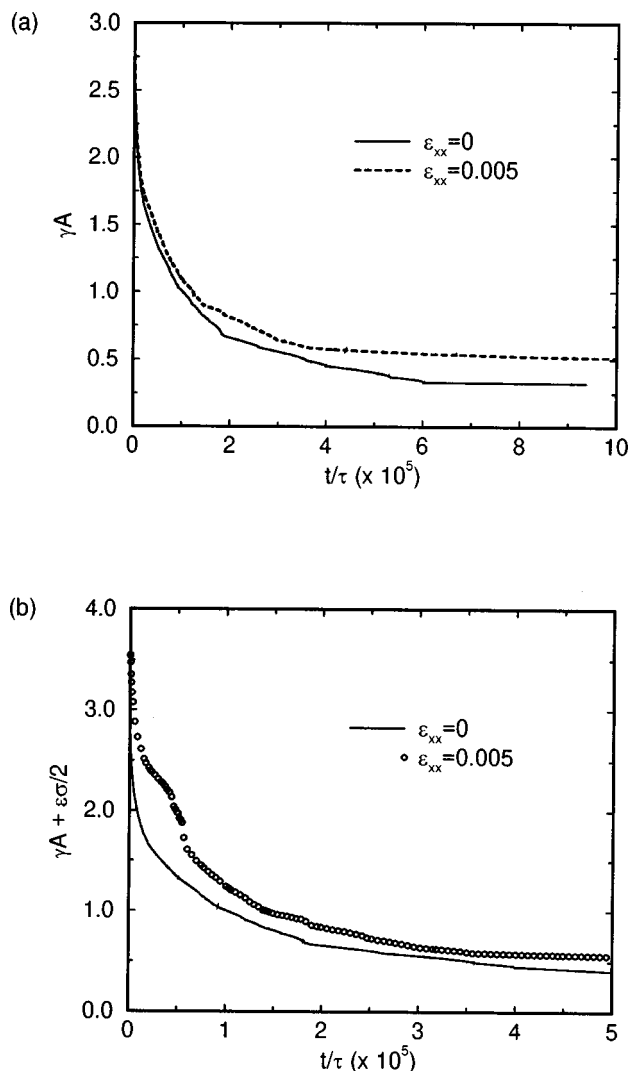


FIG. 8. Reduction with time of (a) surface free energy and (b) total Helmholtz free energy for the trajectories shown in Fig. 7.

extensively in Ref. 1. Here we calculate the time dependence of the surface free energy and the total free energy.

1. Surface free energy and total free energy

For convenience of notation, we refer to the evolution trajectory in the left column of Fig. 7 as \mathcal{T}_0 and that in the right column as $\mathcal{T}_{0.005}$. Figure 8 gives the surface free energy and the total (Helmholtz) free energy, $F = \gamma A + \int_V \epsilon \sigma dV$, as functions of time for both of the trajectories shown in Fig. 7. Under deformation, the surface free energy cannot relax as rapidly as it can without deformation [Fig. 8(a)], even though the deformed system has a higher total free energy than the undeformed one [Fig. 8(b)].

Several salient points may be noted about the plot of F versus time in Fig. 8(b). First, the difference in $F(t=0)$ between $\mathcal{T}_{0.005}$ and \mathcal{T}_0 is equal to the total stored elastic energy in the former. Second, judging from Fig. 7, the curve for $\epsilon_{xx}=0$ should asymptotically approach the value for a straight lamella, i.e.,

$$\lim_{t \rightarrow \infty} F = 2\gamma L = 0.32.$$

Similarly, when $\epsilon_{xx}=0.005$, the severance of the network destroys the connectivity of the solid in the horizontal direction. Since the solid is thereafter surrounded by zero-modulus phase, it is strain-free. The limiting shape is therefore a circle enclosing the same amount of solid as the lamella, so

$$\lim_{t \rightarrow \infty} F = 2\gamma\sqrt{\pi V_s} = 0.49,$$

where V_s is the volume (strictly, area) of solid.

The limiting slopes of the curves as $t \rightarrow 0^+$ in Fig. 8(b) are

$$\lim_{t \rightarrow 0^+} \frac{\tau}{F(t=0)} \frac{dF}{dt} \approx \begin{cases} -34.4 \times 10^5, & \text{for } \mathcal{T}_0, \\ -27.5 \times 10^5, & \text{for } \mathcal{T}_{0.005}. \end{cases}$$

One may view F as an $(N-1)$ -dimensional hypersurface \mathcal{F} in an N -dimensional space, where N is the number of constitutive variables for the system, including the applied strain. Accordingly, the initial states of \mathcal{T}_0 and $\mathcal{T}_{0.005}$ may be thought of as two positions F_0 and $F_{0.005}$ on \mathcal{F} . The evolution traces the steepest monotonically decreasing path on \mathcal{F} consistent with fixed applied strain and the kinetic constraints of motion by SALK. From the fact that F decreases only 2/3 as rapidly along $\mathcal{T}_{0.005}$ as it does along \mathcal{T}_0 , one may infer that the local topography of \mathcal{F} is “shallower” at $F_{0.005}$ than at F_0 —at least along those paths allowed by SALK at fixed applied strain—despite the fact that $F_{0.005} > F_0$.

V. DISCUSSION

Gradient flow concepts²³ have been used to show that motion by $(\kappa - \bar{\kappa})$, that is, by SALK, allows the surface free energy to decrease at a higher rate than does motion by any other volume-conserving mechanism, like surface diffusion (motion by Laplacian of mean curvature for isotropic γ). Previous 2D simulations using this model gave the same result.¹ However, in the present simulations, motion by SALK is equivalent to $(\mu - \bar{\mu})$ rather than $(\kappa - \bar{\kappa})$, the difference being in the contributions to μ of the elastic energy density. Furthermore, there is no one-to-one correspondence between κ and the local strain energy density, since the latter quantity will depend on longer-range structural features of the microstructure such as the connectivity. Trajectory \mathcal{T}_0 in Fig. 7 is motion by $\kappa - \bar{\kappa}$. Therefore, as predicted by Taylor and Cahn²³ and as further demonstrated in Ref. 1, that trajectory is a constrained gradient flow for surface free energy. On the other hand, there is no reason to expect that the same should be true for $\mathcal{T}_{0.005}$. In fact, under any circumstances for which the motion law cannot be written as some function of curvature or of weighted mean curvature,^{23,24} there is no research available to suggest that a gradient flow can be realized.

Srolovitz's stability analysis for sinusoidal perturbations¹³ indicates that the relative contribution to the chemical potential of elastic strain energy, compared to that of surface free energy, should increase with increasing size scale. This should be generally true, regardless of system geometry. One implication of this fact is that the magnitude of elastic defor-

TABLE I. Physical values of the important variables in Fig. 7, assuming system dimensions of $16 \mu\text{m} \times 16 \mu\text{m}$ and $T = 1500 \text{ K}$.

Quantity	Value
Young's modulus, E	100 GPa
Surface free energy density, γ	1 J/m ²
Molar volume, Ω	$8 \times 10^{-5} \text{ m}^3/\text{mol}$

mation required to cause cracklike flaws in sintering powders should increase as the mean particle size decreases, provided the initial microstructural homogeneity remains the same. Thus finer microstructures not only have faster evolution kinetics, but they should be more resistant to dehomogenization by this mechanism.

Can reasonable values of physical parameters cause a trajectory like $\mathcal{T}_{0.005}$? Assuming dimensions of $16 \mu\text{m} \times 16 \mu\text{m}$ and a temperature of 1500 K, the dimensionless variables used in that simulation correspond to physical values shown in Table I. These correspond approximately to the values of γ and E for MgO. Furthermore, a strain of 0.005 could be easily caused by, say, thermal expansion mismatch between two materials over 1000 K, if the coefficients of thermal expansion differ by at least 5×10^{-6} , as they do for Pt/MgO. One might suppose, then, that such phenomena could be important in the high-temperature performance of certain porous thin or thick ceramic films on a metallic substrate.

Some comments are in order on the model itself. First, solid-solid interfaces, including grain boundaries, are not included. The thermodynamics and kinetics become much more complicated when such interfaces are present, particularly if they are incoherent.^{25–27} Thus true sintering/grain growth phenomena, which often involve substantial diffusion of matter along grain boundaries, are not within the scope of the model in its current incarnation. For the same reason, the model does not address diffusional creep along grain boundaries that can cause substantial rearrangement. However, with some minor modifications, the model could account for directional diffusional lattice creep and viscous flow. The possibility of extending this model to allow simulation of important phenomena, such as grain boundary diffusion and interfacial creep, is a subject of continuing inquiry.

As described in the previous sections, digitization of a smooth surface gives rise to local scatter in calculated curvature. Determination of the chemical potential distribution along the corresponding smooth surface is therefore problematic. Although the dynamics of interface motion and stability regimes do not seem to be greatly affected by the scatter, it would be desirable to have a more accurate determination of chemical potential. It may be possible, by averaging over a certain range of neighboring elements, to smooth the calculated chemical potential distribution along a digitized interface. We have chosen to exclude any spatial averaging of the curvature in this work because it introduces another degree of freedom into the calculations, namely the weighted distance over which to average²¹ the boundary values. If averaging were to be included in this model, one could select an “optimum” weighting function using the

condition that the L_2 norm be minimized for a certain model surface geometry, like a sinusoid. However, it is not clear that the same weighting will produce the best results for all possible interface geometries.

The model uses the square pixel elements of a digital image as both volume elements in the mass transport algorithms and as finite elements in the elastic calculations. As mentioned earlier, this leads to the ambiguity of estimating the elastic properties for elements with $0 < \eta < 1$. An adaptive mesh triangulation algorithm would eliminate this ambiguity. A triangulated mesh could always be constructed such that each segment of the ESS would correspond to an edge of a triangular element. Each element then could be taken to have either $\eta = 1$ or 0. Such a nonuniform mesh would have to be recalculated continually as the interfaces evolve, and this process requires substantial computational overhead. But the potential benefit of resolving the strain energy density more accurately at interfaces makes this an attractive alternative which we are currently exploring.

Finally, we comment on the computational resources required to perform simulations like those presented in this article. By far, the most memory-intensive and CPU-intensive portions of the simulations are the finite element calculations. Memory and processing requirements also increase with the number of elements in the system. For the combined ESS/FE simulation shown in the right column of Fig. 7, the memory usage was 15.5 megabytes which averages to about 600 bytes per pixel element. In terms of computational speed, the same simulation used roughly 50 processor hours on a MIPS R4400 chip (250 MHz). We do not claim that the algorithms have been fully optimized for maximum performance, and it is expected that future code refinements will result in substantial increases in performance.

VI. SUMMARY

A new model has been developed that allows one to simulate the combined influences of curvature and elastic energy on the thermodynamics, kinetics, and trajectory of microstructure evolution in two dimensional systems. The model combines an equivalent sharp surface (ESS) approach and a finite element algorithm to calculate the local boundary values of the chemical potential along solidfluid interfaces of arbitrary geometry. Tracking of the interface motion and of topological transformations are handled automatically. We used the model in this article to simulate, for the first time, evolution within a random porous body by a first-order linear interface-reaction kinetic law under these driving forces.

Other rate laws, such as surface diffusion and bulk diffusion, are readily incorporated into the model,^{1,28} and additional driving forces such as thermal gradients can be examined. With the finite element algorithm, one can also track the evolution of macroscopic composite properties, e.g., the effective elastic modulus and effective thermal and electrical conductivities. Such a modeling framework is therefore not only useful for gaining quantitative theoretical insight into these complex dissipation phenomena, but may also be an ideal candidate for integrated process modeling.

ACKNOWLEDGMENTS

We wish to thank Ed Fuller for helpful discussions, and both J. Chuang and A.C. Powell IV for reviewing the manuscript.

APPENDIX A: DIMENSIONLESS VARIABLES

The following dimensionless variables are catalogued here in terms of the groups by which they are defined. The quantities associated with each symbol are given in the text.

Symbol Group

All lengths, L (e.g., λ) $\rightarrow L/\xi$

$\mu \rightarrow \mu/RT$

$\gamma \rightarrow \gamma\Omega/(RT\xi)$

$\kappa \rightarrow \kappa\xi$

$E, K, G \rightarrow E\Omega/RT, K\Omega/RT, G\Omega/RT$

$\sigma \rightarrow \sigma\Omega/RT$

$C \rightarrow k_{\text{SALK}}\Omega\tau/\xi$

APPENDIX B: STRAIN ENERGY DENSITY ALONG A DEFORMED SINUSOIDAL SOLID-FLUID INTERFACE

Asaro and Tiller¹⁰ have given analytical expressions for the stress tensor components in a semi-infinite solid bounded by a sinusoidal surface perturbation:

$$y = a \cos kx.$$

From their expressions, we may evaluate the boundary values of the stress tensor, which yields

$$\sigma_{xx} = \sigma_0 [1 - a(ak^2 \cos kx - 2k)e^{-ak \cos kx} \cos kx], \quad (\text{B1})$$

$$\sigma_{yy} = -a^2 k^2 \sigma_0 \cos kx e^{-ak \cos kx} \cos kx, \quad (\text{B2})$$

$$\sigma_{xy} = -ak \sigma_0 (1 - ak \cos kx) e^{-ak \cos kx} \sin kx, \quad (\text{B3})$$

where σ_0 is the applied stress. The compliance tensor may be written

$$\hat{S} = \begin{pmatrix} \frac{G^2 + GK}{4G^2K} & \frac{G^2 - GK}{4G^2K} & 0 \\ \frac{G^2 - GK}{4G^2K} & \frac{G^2 + GK}{4G^2K} & 0 \\ 0 & 0 & \frac{1}{G} \end{pmatrix}$$

with $K = E/2(1 - \nu)$ and $G = E/2(1 + \nu)$ for plane stress deformations. The elastic strain energy $W = (\hat{\sigma} : \hat{S} : \hat{\sigma})/2$, and upon substitution one obtains

$$\begin{aligned}
 W = & \frac{\sigma_0^2 e^{-2ak \cos kx}}{4GK} \{ (G+K)e^{2ak \cos kx} \\
 & - 4a^2 k^2 [G(e^{ak \cos kx} - 1) - K] \cos^2 kx \\
 & - 4G(2a^3 k^3 \cos^3 kx - a^4 k^4 \cos^4 kx) \\
 & + 4a^2 k^2 K \sin^2 kx + 4ak \cos kx [(G+K)e^{ak \cos kx} \\
 & - 2a^2 k^2 K \sin^2 kx] + a^4 k^4 K \sin^2 2kx \}. \quad (\text{B4})
 \end{aligned}$$

¹J. W. Bullard, J. Appl. Phys. **81**, 159 (1997).

²C. Herring, in *Structure and Properties of Solid Surfaces*, edited by R. Gomer and C. S. Smith (University of Chicago Press, Chicago, 1953), pp. 5–81.

³L. M. Lifshitz and V. V. Slyozov, J. Phys. Chem. Solids **19**, 35 (1961).

⁴C. Wagner, Z. Elektrochem. **65**, 581 (1961).

⁵F. A. Nichols and W. W. Mullins, Trans. AIME **233**, 1840 (1965).

⁶T. K. Gupta, *Crack Healing in Al₂O₃, MgO, and Related Materials*, in *Advances in Ceramics*, Vol. 10, Structure and Properties of MgO and Al₂O₃ Ceramics, edited by W. D. Kingery (American Ceramic Society, Columbus, OH, 1984), pp. 750–766.

⁷F. A. Nichols, J. Mater. Sci. **11**, 1077 (1976).

⁸R. J. Charles and W. B. Hillig, in *Symposium on Mechanical Strength of Glass and Ways of Improving It* (Union Scientifique Continentale du Verre, Belgium, 1962), pp. 511–527.

⁹R. J. Charles and W. B. Hillig, in *High-Strength Materials*, edited by V. F. Zackay (Wiley, New York, 1964), pp. 682–705.

¹⁰R. J. Asaro and W. A. Tiller, Metall. Trans. A **3A**, 1789 (1972).

¹¹J. R. Rice and T.-J. Chuang, J. Am. Ceram. Soc. **64**, 46 (1981).

¹²M. A. Grinfeld, Sov. Phys. Dokl. **31**, 831 (1986).

¹³D. J. Srolovitz, Acta Metall. **37**, 621 (1989).

¹⁴W. H. Yang and D. J. Srolovitz, Phys. Rev. Lett. **71**, 1593 (1993).

¹⁵Y. Wang, H. Wang, L.-O. Chen, and A. G. Khachaturyan, J. Am. Ceram. Soc. **76**, 3029 (1993).

¹⁶Y. Wang, H.-Y. Wang, L.-Q. Chen, and A. G. Khachaturyan, J. Am. Ceram. Soc. **78**, 657 (1995).

¹⁷Y. Wang, L.-Q. Chen, and A. G. Khachaturyan, J. Am. Ceram. Soc. **79**, 987 (1996).

¹⁸E. J. Garboczi and A. R. Day, J. Mech. Phys. Solids **43**, 1349 (1995).

¹⁹W. E. Lorensen and H. E. Cline, Comput. Graph. **21**, 163 (1987).

²⁰J. W. Bullard, E. J. Garboczi, W. C. Carter, and E. R. Fuller, Jr., Comput. Mater. Sci. **4**, 103 (1995).

²¹W. W. Mullins, in *Metal Surfaces: Structure, Energetics, and Kinetics* (ASM, Metals Park, OH, 1963), pp. 17–64.

²²R. E. Newnham, D. P. Skinner, and L. E. Cross, Mater. Res. Bull. **13**, 525 (1978).

²³J. E. Taylor and J. W. Cahn, J. Stat. Phys. **77**, 183 (1994).

²⁴J. E. Taylor, Acta Metall. Mater. **40**, 1045 (1992).

²⁵F. C. Larché and J. W. Cahn, Acta Metall. **33**, 331 (1985).

²⁶M. E. Gurtin, Arch. Ration. Mech. Anal. **123**, 305 (1993).

²⁷P. Cermelli and M. E. Gurtin, Arch. Ration. Mech. Anal. **127**, 41 (1994).

²⁸J. W. Bullard, Mater. Sci. Eng. A **238**, 128 (1997).